IJMMM International Journal of Minerals, Metallurgy and Materials 矿物冶金与材料学报（英文版）

Optimization of Eu-doped lanthanum tungstate nanophosphors via surface modification for superior red luminescence and photonic applications

K. Naveen Kumar, L. Vijayalakshmi, P.K. Vishwakarma, Jiseok Lim, Mohammad Rezaul Karim, Ibrahim A. Alnaser, and D. Rajesh

Cite this article as:
K. Naveen Kumar, L. Vijayalakshmi, P.K. Vishwakarma, Jiseok Lim, Mohammad Rezaul Karim, Ibrahim A. Alnaser, and D. Rajesh, Optimization of Eu-doped lanthanum tungstate nanophosphors via surface modification for superior red luminescence and photonic applications, *Int. J. Miner. Metall. Mater.*, 32(2025), No. 10, pp. 2579-2591. https://doi.org/10.1007/s12613-025-3212-9

View the article online at SpringerLink or IJMMM Webpage.

INTERNATIONAL JOURNAL OF
Minerals, Metallurgy and Materials

Volume 32, Number 10, October 2025
Page 2579

Research Article

https://doi.org/10.1007/s12613-025-3212-9

Optimization of Eu-doped lanthanum tungstate nanophosphors via surface modification for superior red luminescence and photonic applications

K. Naveen Kumar[1),*,✉], *L. Vijayalakshmi*[1),*,✉], *P.K. Vishwakarma*[2)], *Jiseok Lim*[1),✉], *Mohammad Rezaul Karim*[3)], *Ibrahim A. Alnaser*[3)], *and D. Rajesh*[4)]

1) School of Mechanical Engineering, Yeungnam University, Gyeongsan, Gyeongbuk 38541, Republic of Korea
2) Department of Physics, Institute of Science, Banaras Hindu University, Varanasi 221005, India
3) Center of Excellence for Research in Engineering Materials (CEREM), Deanship of Scientific Research, King Saud University, Riyadh 11421, Saudi Arabia
4) Department of Physics, Madanapalle Institute of Technology and Science, Madanapalle, India
(Received: 18 March 2025; revised: 15 June 2025; accepted: 18 June 2025)

Abstract: The luminescence behavior of Eu^{3+}-activated lanthanum tungstate nanophosphors exhibiting intense red emission was systematically explored by modifying their surfaces using various agents, including polyvinylpyrrolidone (PVP), cetyltrimethylammonium bromide (CTAB), trisodium citrate (TC), polyvinyl alcohol (PVA), and ethylene glycol (EG). These nanophosphors were synthesized via a facile hydrothermal-assisted solid-state reaction. X-ray diffraction (XRD) analysis confirmed the orthorhombic crystal structure of all the prepared samples. Morphological and size analyses were performed using scanning electron microscopy (SEM) and particle size distribution profiling. High-resolution transmission electron microscopy (HRTEM) complemented by elemental mapping was used to evaluate the particle dimensions and interplanar spacing of the optimized sample. Fourier-transform infrared spectroscopy (FTIR) was used to identify functional groups and assign corresponding vibrational bands. X-ray photoelectron spectroscopy (XPS) provided insights into the elemental composition and binding energies of the optimized nanophosphors. Notably, the PVA-modified sample doped with 14mol% Eu^{3+} exhibited pronounced red emission at 616 nm, attributed to the $^5D_0 \rightarrow {}^7F_2$ electric dipole transition of Eu^{3+} ions under ultraviolet (UV) excitation. Detailed excitation and emission spectral analyses were performed, with band assignments corresponding to the relevant electronic transitions. Among the surface-treated variants, the PVA-modified nanophosphors demonstrated exceptional color purity of 99.6%, international commission on illumination (CIE) chromaticity coordinates of (0.6351, 0.3644), and a correlated color temperature of 1147 K. These superior optical features are ascribed to the enhanced surface passivation and suppression of nonradiative recombination, facilitated effectively by the PVA surface layer. Lifetime decay analysis across all samples revealed a significantly extended lifetime for the optimized composition, further supporting its superior luminescence efficiency. In addition, evaluation of the biocompatibility of the nanophosphors highlighted their potential for biomedical applications. Overall, these findings emphasize the efficacy of PVA-modified Eu^{3+}-doped lanthanum tungstate nanophosphors as highly efficient red emitters, suitable for application in white light-emitting diodes (WLEDs) and latent fingerprint detection while offering valuable insights into the role of surface modification in tuning the optical properties of nanophosphors.

Keywords: nanophosphors; surface modifiers; PVA; photoluminescence; cytotoxicity

1. Introduction

The features of nanomaterials doped with rare-earth elements, including their extremely small particle size, high luminescence quantum yield, and photostability, make them indispensable for a wide range of technologies. These advances are also applicable to the unique properties of certain materials known as nanophosphors with bright light-emitting potentials, a subset commonly referred to as fluorescent down-shifting phosphors, ranging from lighting applications through the health and biosciences, including omics technologies [1]. Although traditional nitride and sulfide phosphors are widely used, their poor chemical stabilities and sensitivities to moisture make them unsuitable alternatives to organic luminescent probes [2–3]. Because nitride and oxynitride phosphors are mostly good emitters of red luminescence, they are difficult to synthesize using procedures that involve high temperatures for extended periods of time [4]. Oxide-based phosphors, which have higher brightness and environmental stability in that they are resistant to moisture, are one of the most attractive phosphor materials for photonic applications, and they are also relatively free from hazardous toxic elements. They also emit high-purity red light under near-ultraviolet (NUV) excitation [5]. The efficiency of phosphor

* These authors contributed equally to this work.
✉ Corresponding authors: K. Naveen Kumar E-mail: knaveenphy@gmail.com; L. Vijayalakshmi E-mail: lvl.phy@gmail.com; Jiseok Lim E-mail: jlim@yu.ac.kr

Springer

absorption is strongly dependent on the host matrix and luminescent centers (>5%), particularly molybdates, vanadates, and tungstates (up to 100%); other factors cause charge transfer from the host lattice to lanthanide ions [6]. Among these, tungstates have gained prominence because of their self-promoting luminescence, excellent thermal and chemical stabilities, and established application in scintillation detectors, solid-state lasers, and stimulated Raman scattering [7–8]. Although traditional red phosphors such as $Y_2O_2S:Eu^{3+}$ and $Y_2O_3:Eu^{3+}$ are well-known, their poor NUV and blue absorption necessitates efficient sensitization from the host to the Eu^{3+}ions [9–10]. Tungstates activated by rare-earth ions are characterized by strong covalent bonds and offer both high stability and exceptional luminescence [11].

Among the various phosphors used for photonic applications, inorganic nanophosphors doped with rare-earth ions are of interest because of their facile synthesis and outstanding chemical stability. The enhanced properties of these materials have raised the size-dependent structure–property relationship to a new level and have enabled more widespread application in electronics, photonics, and health care [12]. To the best of our knowledge, this is the first study to investigate $La_{10}W_{22}O_{81}$ (LWO) as a novel host matrix for the incorporation of lanthanide ions. LWO nanophosphor systems that have been doped with rare-earth ions and synthesized using various chelating agents have not yet been reported. The exceptional fluorescence observed from these lanthanide-based nanophosphors is attributed to the high energy levels and distinctive intra-4f–4f electronic transitions of the lanthanide ions. These transitions produce intense emission lines characterized by long lifetimes and sharp absorption bands extending from the ultraviolet to the infrared regions [13]. Among the lanthanide ions, Eu^{3+} is a particularly suitable red-emitting activator because of its distinctive spectral properties, including narrow emission and excitation bands, a large Stokes shift, a prolonged luminescence lifetime, and exceptional color purity. These characteristics are attributed to intraconfigurational f–f transitions within the crystal lattice under NUV excitation [14].

The high-temperature synthesis of lanthanide-doped nanoparticles often results in clustering of the optically active lanthanide ions, leading to agglomeration and decreased luminescence owing to energy loss through cross-relaxation and nonradiative pathways. The incorporation of capping agents that enable redispersion in water and organic solvents can mitigate this problem. Compared to bulk phosphors, nanophosphors offer improved efficiency in display and lighting applications by reducing internal scattering. However, as the particle size decreases, the surface-to-volume ratio increases, leading to the formation of surface defects [15–17]. These defects, such as dangling bonds at grain boundaries, distorted crystal lattices, and organic groups like hydroxyl and carboxylate, can reduce the luminescence efficiency by creating nonradiative relaxation centers [18]. The defects can be mitigated by using suitable agents to effectively modify the surfaces such that they have fewer imperfections. Understanding the influence of surface modification on the photoluminescence properties of nanoparticles is essential for optimizing their emission characteristics for advanced white light-emitting diode (LED) applications [19].

Recent studies have focused extensively on elucidating the mechanisms of surface modification [20–21]. Controlled synthesis techniques employing surfactants are important for exploring and controlling crystal morphologies. These surfactants significantly influence the size, shape, crystallinity, and other critical properties of inorganic nanocrystals. Commonly employed surfactants include trisodium citrate, sodium dodecyl sulfate (SDS), oleic acid, ethylenediamine tetraacetic acid (EDTA), cetyltrimethylammonium bromide (CTAB), dimethylformamide (DMF), sodium bis(2-ethylhexyl) sulfosuccinate (AOT), polyvinylpyrrolidone (PVP), triethyl orthosilicate (TEOS), tetraethoxysilane (TOX), triethanolamine (TEA), glycine, and oleylamine [22–25]. The molecular architecture of surfactants typically comprises hydrophilic head and hydrophobic tail. To minimize contact with water, the hydrophobic tails aggregate, whereas surfactants with relatively large heads and smaller tails form micelles characterized by hydrophobic core and hydrophilic shell [26]. As previously reported, the preparation of Eu^{3+}-doped lanthanum tungstate nanophosphor materials combines hydrothermal and solid-state techniques and uses trisodium citrate dihydrate as the surfactant [27]. Building on this foundation, this study explored the modulation of the surface morphology of the phosphorescent material using various chelating agents, including ethylene glycol (EG), trisodium citrate (TC), CTAB, PVP, and polyvinyl alcohol (C_2H_4O, PVA). This study entails a comprehensive and systematic investigation of the luminescence properties of nanophosphors, and the findings shed light on the impact of surface morphology alterations induced by different chelating agents.

2. Experimental

2.1. Preparation of materials

Eu-doped lanthanum tungstate phosphors were synthesized by a combination of hydrothermal and solid-state reactions. The hydrothermal process was employed to promote particle uniformity and minimize surface defects. Subsequent sintering enhanced the luminescence intensity and thermal stability of the phosphor. High-purity lanthanum nitrate hexahydrate ($La(NO_3)_3{\cdot}6H_2O$) of 1.564 g, ammonium metatungstate hydrate ($(NH_4)_6H_2W_{12}O_{40}{\cdot}xH_2O$) of 0.259 g, trisodium citrate dihydrate ($Na_3C_6H_5O_7{\cdot}2H_2O$, chelating agent) of 0.050 g, and europium nitrate pentahydrate ($Eu(NO_3)_3{\cdot}5H_2O$) of 0.252 g were procured from Sigma-Aldrich. The precursors were dissolved in deionized water and subjected to continuous magnetic stirring for 1 h at room temperature to obtain a homogeneous solution. The precursor solution was subsequently heated in a Teflon-lined stainless-steel autoclave at 200°C for 24 h to form the product via hydrothermal synthesis. The resulting precipitate was purified through successive washing with deionized water and ethanol, followed by

drying at 90°C for 12 h. The final nanophosphor powder was obtained by calcination of the dried product at 900°C for 6 h. The powder was subsequently stored for characterization.

Chelating agents influence the nucleation, growth, and crystallinity by coordinating with the precursor ions, which serves to control the particle dispersion and minimize surface defects. In this study, PVA, PVP, CTAB, TC, and EG were used as chelating agents to tailor the structural and optical properties of the Eu^{3+}-doped LWO nanophosphors. During the hydrothermal reaction, the chelating agents interact with the La^{3+} and W^{6+} ions to form complex intermediates, thus preventing uncontrolled agglomeration. The boiling/decomposition temperatures of all the chelating agents are below 320°C, which enabled them to interact during the hydrothermal reaction (200°C) to regulate precursor complexation and particle dispersion. Upon calcination at 900°C, these organic molecules decompose, leaving behind their structural influences, such as controlled grain size and defect passivation.

2.2. Characterization

The crystalline structures of the lanthanum tungstate samples doped with Eu were elucidated by X-ray diffraction analysis (XRD, SEIFERT 303 TT diffractometer with Cu K_α radiation). The morphological features of the nanophosphor containing 14mol% Eu were examined using field-emission scanning electron microscopy (FE-SEM, Hitachi S-4800, Japan). The particle size and shape were determined using transmission electron microscopy (TEM, Hitachi H-7600, Japan). A more in-depth analysis was conducted by acquiring high-resolution TEM images (HRTEM, FEI Titan G2 field emission microscope operating at 200 kV, USA), selected area electron diffraction (SAED) patterns, and SEM images with a high-angle annular dark field (HAADF) detector.

The elemental compositions and oxidation states of the phosphor samples were determined using X-ray photoelectron spectroscopy (XPS) on a Thermo Scientific K_α spectrometer. The photoluminescence (PL) spectra of the Eu-doped phosphors were recorded using a SCINCO FluoroMate FS-2 visible fluorescence spectrometer. The excited-state lifetimes of the Eu ions in the 5D0 energy level were measured at room temperature using an Agilent Cary Eclipse spectrometer. The absolute quantum efficiencies of the nanophosphors were evaluated using an integrating sphere interfaced with an Edinburgh Instruments FLS900 fluorescence spectrometer.

3. Results and discussion

3.1. Structural investigation

The crystalline structures of the synthesized Eu^{3+}-doped LWO nanophosphors were determined by recording conventional XRD patterns in the range 10°−50° with Cu K_α radiation (λ = 1.5406 Å). The obtained diffractograms were subsequently compared to the standard JCPDS data to identify the phase composition. As shown in Fig. 1(a)–(f), the XRD patterns of the Eu^{3+}-doped LWO nanophosphors prepared

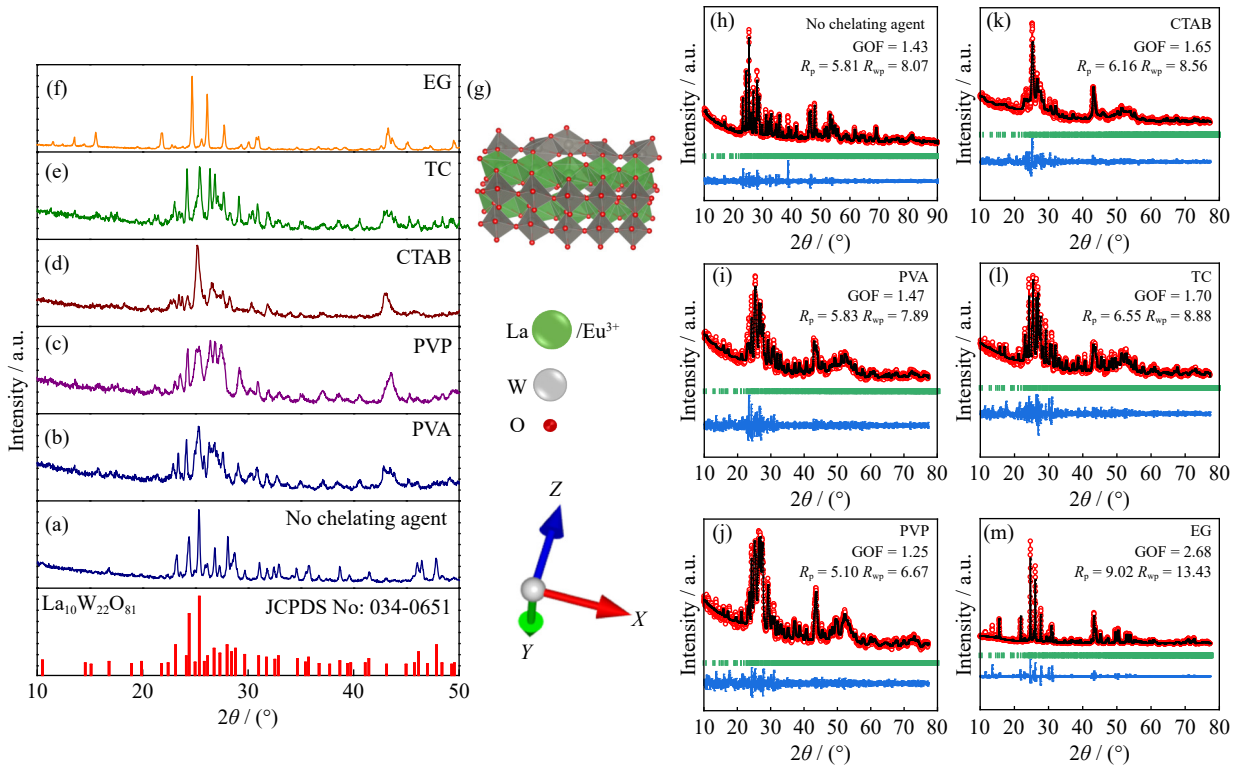

Fig. 1. XRD patterns of (a) Eu^{3+} (14mol%)-doped LWO without chelating agent, (b) Eu^{3+} (14mol%)-doped LWO with PVA, (c) Eu^{3+} (14mol%)-doped LWO with PVP, (d) Eu^{3+} (14mol%)-doped LWO with CTAB, (e) Eu^{3+} (14mol%)-doped with TC, (f) Eu^{3+} (14mol%)-doped LWO with EG. (g) Crystal structure of the LWO compound. Rietveld refinement of XRD patterns of (h) Eu^{3+} (14mol%)-doped LWO without chelating agent, (i) Eu^{3+} (14mol%)-doped LWO with PVA, (j) Eu^{3+} (14mol%)-doped LWO with PVP, (k) Eu^{3+} (14mol%)-doped LWO with CTAB, (l) Eu^{3+} (14mol%)-doped LWO with TC, and (m) Eu^{3+} (14mol%)-doped LWO with EG.

with various chelating agents (PVA, PVP, CTAB, TC, and EG) and without chelating agent exhibit characteristic diffraction peaks that align well with the orthorhombic structure of the LWO host matrix, consistent with the space group Pbcn (60), as previously reported in our work [28]. Notably, no extraneous peaks indicative of impurity phases were discernible within the detectable XRD range, suggesting the successful formation of phase-pure LWO nanophosphors [29]. The differences in the diffraction peak intensities were attributed to variations in the crystallite size and strain induced by different chelating agents, rather than to phase impurities. Furthermore, no impurity phases were observed following the addition of the chelating agents to LWO, suggesting that the Eu^{3+} ions and chelating agents did not alter the fundamental structure of the host and were fully integrated into the LWO lattice [30]. We attributed this successful incorporation to the similar ionic radii (r_{Eu} = 0.95 Å, r_{La} = 1.06 Å) and identical charge states (+3) of Eu^{3+} and La^{3+} ions [31–32]. The crystal structure of LWO compound is clearly depicted in Fig. 1(g).

In addition to conventional phase identification, detailed structural insights were obtained through Rietveld refinement of XRD patterns, as shown in Fig. 1(h)–(m). Refinement was performed using the FullProf suite by employing the orthorhombic structure of $La_{10}W_{22}O_{81}$ (space group Pbcn (60)) as the starting model, which is consistent with the reference (JCPDS No. 034-0651). The refined patterns (red solid lines) exhibited excellent agreement with the experimental data (black open circles), and the minimal difference profiles (blue lines) confirmed the high accuracy of the fitting. The sharp and well-defined peaks indicated the high crystallinity of the as-synthesized samples.

The refinement parameters, such as the weighted profile *R*-factor (R_{wp}), expected *R*-factor (R_{exp}), and goodness-of-fit (GOF, χ^2) remained within acceptable limits, suggesting reliable refinement quality for all samples, which are listed in Table S1 (see the Supplementary Information). The absence of unidentified peaks in the difference plots also supports the phase purity of the Eu^{3+}-activated LWO samples, irrespective of the chelating agent used. Notably, the slight changes in the peak intensities and widths observed among the different chelating agent-assisted samples were attributed to their influence on the microstrain and crystallite growth dynamics during synthesis.

The lattice parameters extracted from the refinement exhibited marginal variations across the samples, indicating that the inclusion of Eu^{3+} ions and chelating agents had a negligible effect on the crystal symmetry of the host. This preservation of structural integrity is attributed to the closely corresponding ionic radii and valences of La^{3+} (1.06 Å) and Eu^{3+} (0.95 Å), which facilitate effective substitution without inducing lattice distortion. The unit cell volume showed minor deviations, possibly linked to the local strain fields generated during thermal treatment or differences in the coordination interactions introduced by the chelating species.

Overall, the Rietveld refinement confirmed the successful stabilization of the orthorhombic LWO framework and validated the homogeneous incorporation of Eu^{3+} ions within the host lattice. These results corroborate the earlier phase identification analysis and establish the structural robustness of the synthesized nanophosphors in different chemical environments.

3.2. FE-SEM analysis

FE-SEM images of the LWO nanophosphors doped with Eu^{3+} (14mol%) and synthesized using the different chelating agents are presented in Fig. 2.

The nanophosphors were synthesized by incorporating EG, TC, CTAB, PVP, and PVA. These chelating agents significantly influence the morphology and particle size distribution of the resulting nanophosphors. Fig. 2(a) shows that the nanophosphors synthesized using EG exhibited a relatively uniform distribution with particle sizes predominantly in the micrometer range. The particles appeared to be well-dispersed, indicating that EG effectively prevented agglomeration during the synthesis process [33]. When TC was used as the chelating agent, the FE-SEM image revealed a slight increase in particle aggregation compared to the EG sample, as shown in Fig. 2(b). The particles were still predominantly nano-sized, but there was evidence of some larger cluster formation, which might be attributed to the interaction between trisodium citrate and the precursors [34]. Fig. 2(c) shows that the nanophosphors synthesized with CTAB presented a distinct morphology characterized by a more significant degree of aggregation, and the particles were smaller than those in the EG sample and slightly larger than those in the TC phosphor. This suggests that CTAB may not be as effective in controlling the particle size and preventing agglomeration under the conditions used in our observations [35]. Fig. 2(d) shows that the use of PVP as a chelating agent resulted in a remarkable reduction in particle size with a highly uniform distribution. The particles were well dispersed, indicating that PVP is highly effective in stabilizing the nanoparticles and preventing agglomeration, likely because of its steric stabilization properties [36]. The morphology was found to consist of micro sized spheres with a rumpled grass surface, which comprised numerous nanosized agglomerated particles, as shown in Fig. 2(d). In the case of PVA (Fig. 2(e)), the morphology was similar to that obtained with PVP, with well-dispersed and uniformly sized nanoparticles. PVA appears to be almost as effective as PVP in controlling the particle size and distribution, although the surface morphology of the particles may differ slightly [37]. The particle size was determined to be (138 ± 2) nm, as shown in Fig. 2(e). The superior performance of PVA-assisted nanophosphors can be attributed to their dual roles as chelating and stabilizing agents. PVA effectively binds to precursor ions, preventing uncontrolled particle growth while simultaneously passivating surface defects, thereby enhancing the luminescence efficiency. The ability of PVA to form uniform polymeric network around the nanoparticles minimizes agglomeration, leading to narrower and more homogenous particle distribution, as evid-

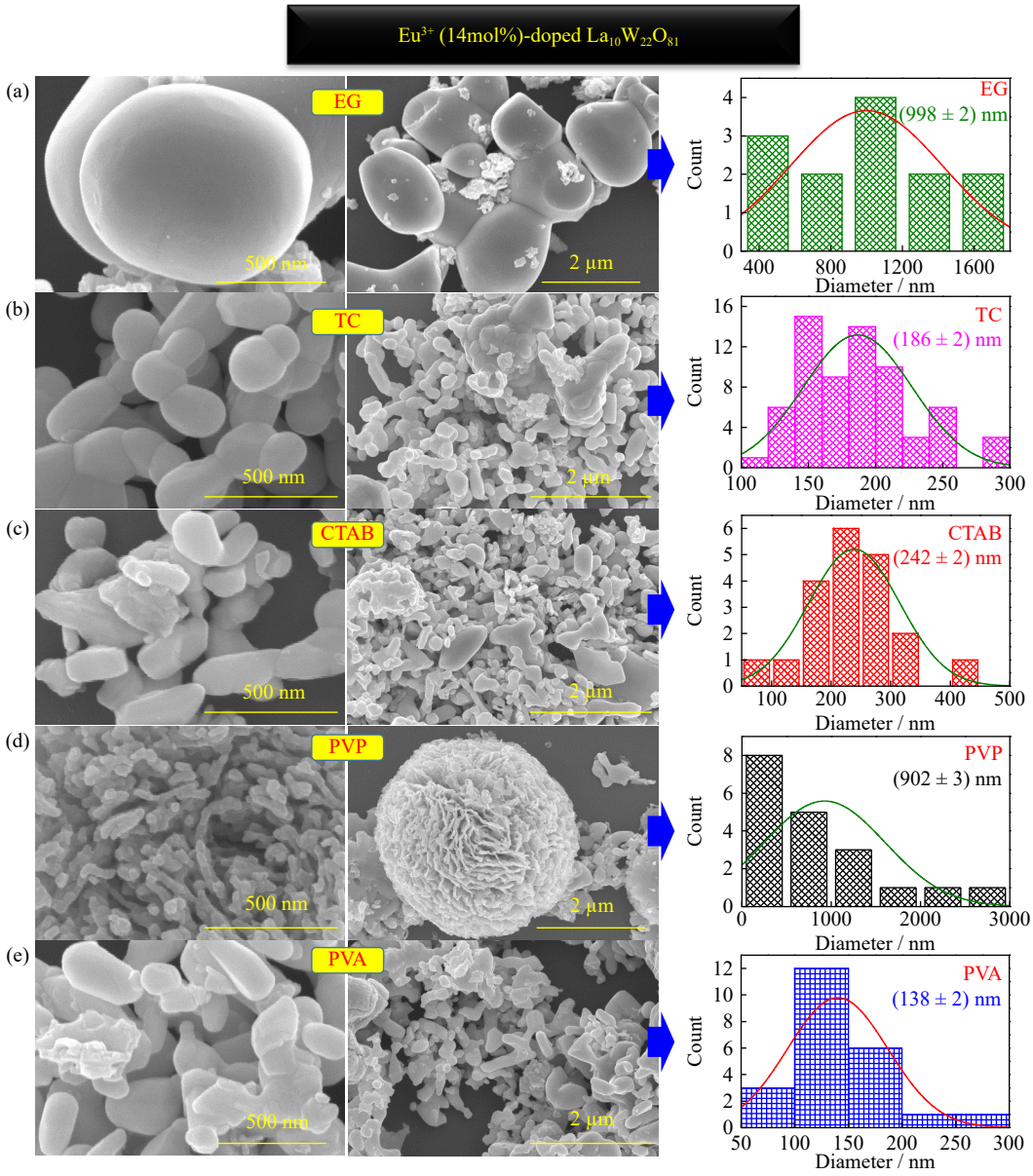

Fig. 2. FE-SEM images and the particle distribution of Eu^{3+} (14mol%)-doped LWO nanophosphor synthesized using the chelating agents of (a) EG, (b) TC, (c) CTAB, (d) PVP, and (e) PVA.

enced by the results of the FE-SEM and TEM analyses in Section 3.3. The particle distribution profiles accompanying the FE-SEM images quantitatively confirm these observations. The narrowest and most uniform particle size was obtained for the sample synthesized with PVA, whereas those synthesized with EG produced larger particles, and those synthesized with CTAB formed more aggregated particles. These results indicate that the choice of the chelating agent plays a crucial role in determining the final morphology and particle size distribution of the Eu^{3+}-doped LWO nanophosphors, with PVA being particularly effective in producing well-dispersed nanoscale particles.

3.3. TEM analysis

Fig. 3 shows the TEM, dark-field TEM, HRTEM, and elemental mapping analyses of the Eu^{3+} (14mol%)-doped LWO nanophosphors synthesized using PVA as the chelating agent. The particles exhibit irregular shapes with some degree of aggregation, as shown in Fig. 3(a). The average particle size was in the nanometer range, indicating the effective formation of nanoscale phosphors via the PVA-assisted synthesis route. The dark-field TEM image provided enhanced contrast, highlighting the individual nanoparticles more distinctly, as shown in Fig. 3(b). This imaging technique emphasizes the edges and boundaries of the particles, confirming their irregular morphology and revealing additional structural details that are not as clear in the bright-field TEM images. The HRTEM image presents lattice fringes with a measured interplanar spacing of approximately 0.57 nm as depicted in Fig. 3(c). This high-resolution analysis indicated the crystalline nature of the nanoparticles and allowed for the identification of specific crystallographic planes. The clear and regular lattice fringes suggested a high degree of crystallinity in the Eu^{3+}-doped LWO nanophosphors.

The elemental mapping images show the distributions of La, W, O, and Eu within the nanophosphors (Fig. 3(d)). The

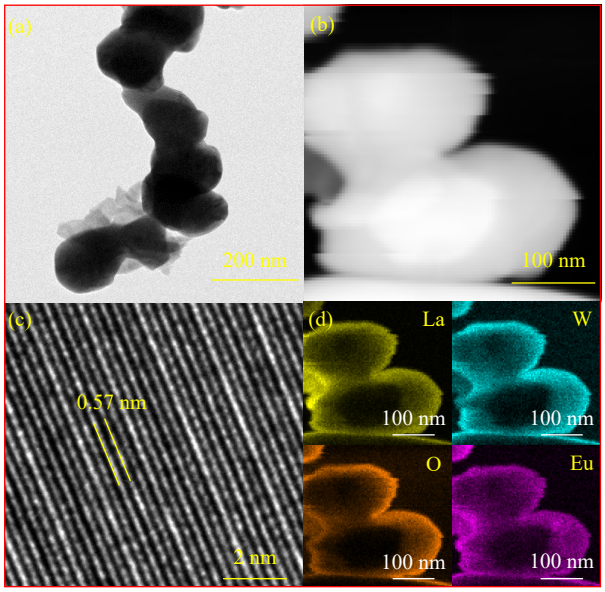

Fig. 3. (a) TEM, (b) dark-field TEM, (c) HRTEM, and (d) elemental mappings of the Eu^{3+} (14mol%)-doped LWO nanophosphor using PVA as chelating agent.

uniform distribution of these elements confirmed that the LWO matrix had been successfully doped with Eu^{3+} ions. The consistent presence of these elements throughout the sample suggests the homogeneity and effective incorporation of dopant ions during the synthesis process. Collectively, these analyses provide a comprehensive understanding of the structural and compositional characteristics of the LWO nanophosphors doped with Eu^{3+} (14mol%). The TEM and dark-field TEM images reveal the overall morphology and particle size, whereas the HRTEM image confirms the crystalline nature of the nanoparticles. Elemental mapping underscores the uniform distribution of the dopants, highlighting the successful synthesis of homogeneously doped nanophosphors using PVA as the chelating agent.

3.4. FTIR analysis

Fig. 4 shows the FTIR spectra of the LWO and Eu^{3+} (14mol%)-doped LWO nanophosphors using PVA as the chelating agent. The FTIR spectra provided insights into the vibrational modes and functional groups present in the nanophosphor samples, allowing for the detailed characterization of their chemical structures. The spectra exhibit several characteristic peaks that are indicative of the vibrational modes of the constituent elements and compounds within the nanophosphors. The LWO spectrum gives rise to a broad absorption band around 564 cm^{-1}, which is attributed to the W−O stretching vibrations in the tungsten oxide matrix [38]. Additional peaks at 688, 718, and 783 cm^{-1} correspond to various vibrational modes of the WO_3 lattice [39]. The spectrum of the doped sample had similar peaks but with slight shifts and changes in intensity owing to the incorporation of Eu^{3+} ions and the presence of PVA as the chelating agent. The peak at 931 cm^{-1} is associated with the W–O stretching vibrations in the WO_4 tetrahedral units of the LWO host lattice [40]. The peaks at 480 and 564 cm^{-1} in the doped sample are consistent with those in the LWO spectrum, reaffirming the presence of W–O bonds [41]. The minor shifts and intensity variations in the peaks suggest interactions between the Eu^{3+} ions and the tungsten oxide matrix, as well as possible modifications due to the PVA chelating agent. A comparison of the FTIR spectra of the LWO and Eu^{3+}-doped LWO nanophosphors demonstrates the successful incorporation of Eu^{3+} ions and provides evidence of the structural integrity of the tungsten oxide matrix. The presence of characteristic peaks for both the W–O and Eu–O bonds confirmed the effective doping process, whereas the minor spectral shifts highlighted the influence of the chelating agent on the overall structure. This FTIR analysis underscores the potential of using PVA as an effective chelating agent in the synthesis of Eu^{3+}-doped LWO nanophosphors by ensuring the homogeneous distribution and stable incorporation of dopant ions.

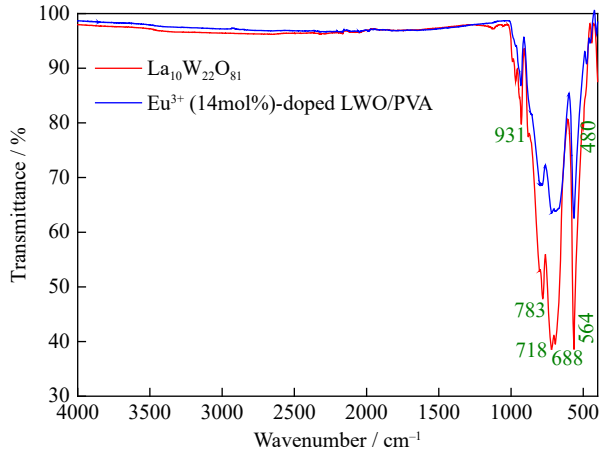

Fig. 4. FTIR spectra of LWO and Eu^{3+} (14mol%)-doped LWO nanophosphors with PVA as the chelating agent.

3.5. XPS analysis

The Eu^{3+}-doped LWO nanophosphors synthesized using PVA as the chelating agent were analyzed using XPS to elucidate the elemental composition and oxidation states of the constituent elements. Survey spectra spanning a binding-energy range of 0–1350 eV and high-resolution spectra focused on the core-level regions of La 3d, W 4f, O 1s, and Eu 3d were acquired. The presence of these core-level signals in the survey spectrum (Fig. 5(a)) confirmed the successful incorporation of La, W, O, and Eu within the nanophosphor matrix. The core-level spectra of each element exhibited distinct binding energy peaks corresponding to their respective oxidation states.

The La 3d region (830–860 eV) is characterized by multiple peaks, as shown in Fig. 5(b). The La $3d_{3/2}$ peaks appear at 855.48 and 851.30 eV, while the La $3d_{5/2}$ peaks are observed at 838.47 and 834.45 eV. These peaks are consistent with the La^{3+} oxidation state, indicating the successful doping of the matrix with La [42–43]. In the W 4f region (32–45 eV), peaks appear at 37.45 eV ($4f_{7/2}$), 35.27 eV ($4f_{5/2}$), and a low-intensity peak at 40.1 eV, attributed to W^{6+} (Fig. 5(c)). The well-resolved doublets confirm the +6-oxidation state of tungsten,

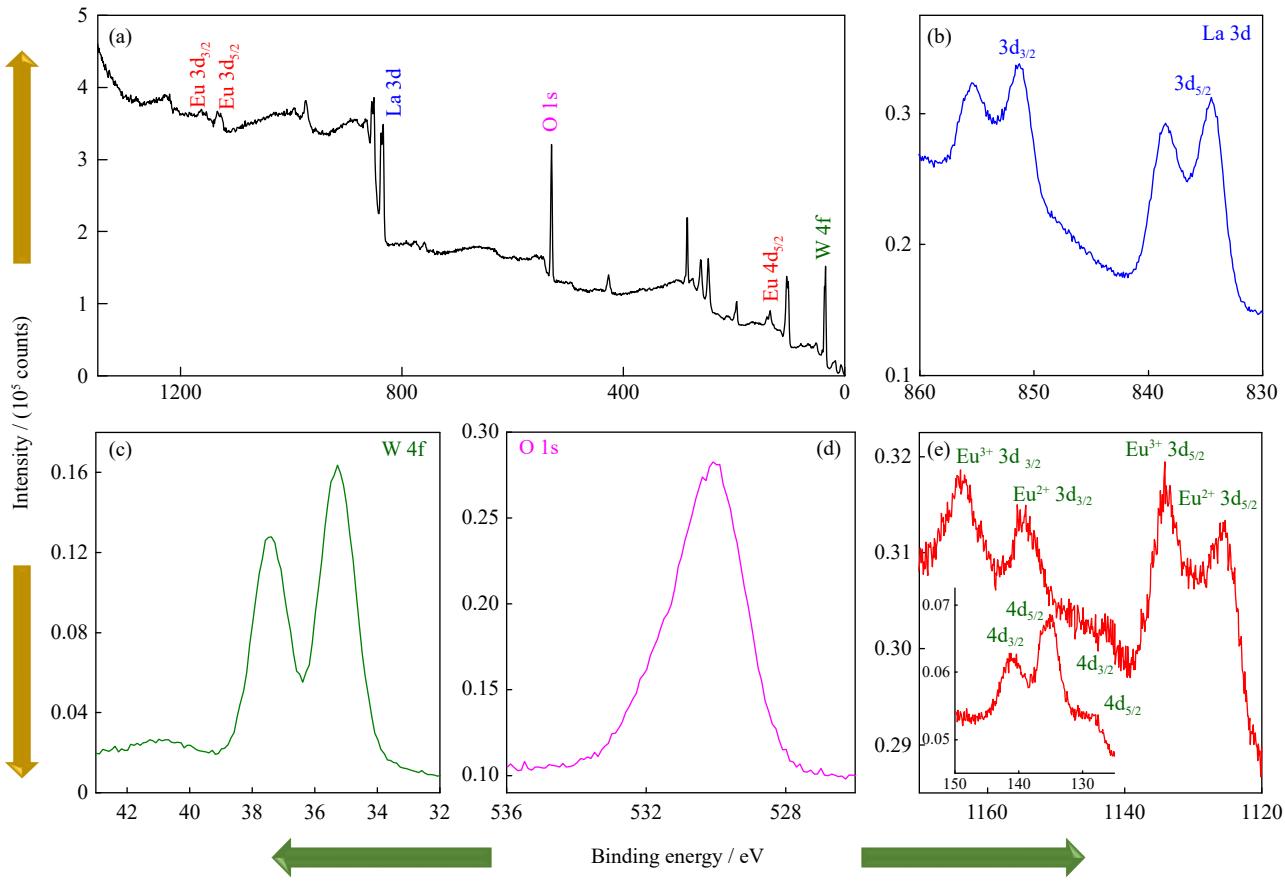

Fig. 5. XPS spectra of Eu^{3+} (14mol%)-doped LWO nanophosphor using PVA as chelating agent: (a) survey spectrum; (b) La 3d; (c) W 4f; (d) O 1s; (e) Eu 3d (inset of Eu 4d).

which is essential for maintaining the charge balance in the compound. Fig. 5(d) shows the O 1s spectrum (526–538 eV) displayed a prominent peak at 530 eV, with an additional peak at 532.02 eV [44]. These peaks correspond to the lattice oxygen in $La_{10}W_{22}O_{81}$ and possibly to surface-adsorbed oxygen species or hydroxyl groups. The Eu 3d and 4d regions exhibited several significant peaks. The Eu $3d_{3/2}$ peaks at 1163.89 and 1154.48 eV, and the Eu $3d_{5/2}$ peaks at 1142.56, 1134.04, and 1125.53 eV suggest the presence of Eu^{3+} [45–46], as shown in Fig. 5(e). The inset of Eu 4d region further supports this with peaks at 141.22, 136.71, 135.08, and 128.42 eV. The XPS analysis conclusively identifies the oxidation states and confirms that the $La_{10}W_{22}O_{81}$ nanophosphor had been successfully doped with La, W, O, and Eu. The binding energies were consistent with the expected values for the La^{3+}, W^{6+}, and Eu^{3+} states. This comprehensive spectral analysis is crucial for understanding the electronic structures and chemical environments of the synthesized nanophosphors, which is essential for their potential applications in luminescent devices.

3.6. Photoluminescence, lifetime, and color purity studies of Eu^{3+}-doped LWO nanophosphors with various chelating agents

In our previous study [27], we synthesized Eu^{3+}-doped LWO nanophosphors and systematically investigated their luminescence properties to determine the Eu^{3+} concentration that generates the optimal emission. These findings revealed that a doping concentration of 14mol% yielded the most favorable luminescence characteristics. Building on this foundation, the present work explores the impact of various chelating agents on the surface modification and evaluates their influence on the luminescence performance of Eu^{3+} (14mol%)-doped LWO nanophosphors. The photoluminescence excitation spectra of the optimized Eu^{3+} (14mol%)-doped LWO nanophosphors synthesized without and with the different chelating agents are presented in Fig. 6(a). These spectra were recorded at an emission wavelength of 616 nm within the spectral range of 335–450 nm. The distinct excitation bands observed at 362, 374, 382, 395, and 416 nm correspond to electronic transitions from the ground state ($^7F_0$) to the excited states ($^5D_4$, $^5H_6$, $^5L_7$, $^5L_6$, and $^5D_3$) [47]. Among these, the most intense excitation band was centered at 395 nm ($^7F_0 \rightarrow {}^5L_6$), indicating a strong excitation capability when coupled with UV LED chips, which emit near 400 nm. The presence of an $O^{2-} \rightarrow Eu^{3+}$ charge transfer transition is crucial in Eu^{3+}-doped oxides and typically occurs below 300 nm as displayed in Fig. S1. Our previous study [27] on the same material without the chelating agents included a detailed discussion of this charge transfer process and its impact on the luminescence properties.

Among the various chelating agents that were used, the PVA-assisted nanophosphors exhibited the highest excitation intensity, indicating greater emission, as shown in

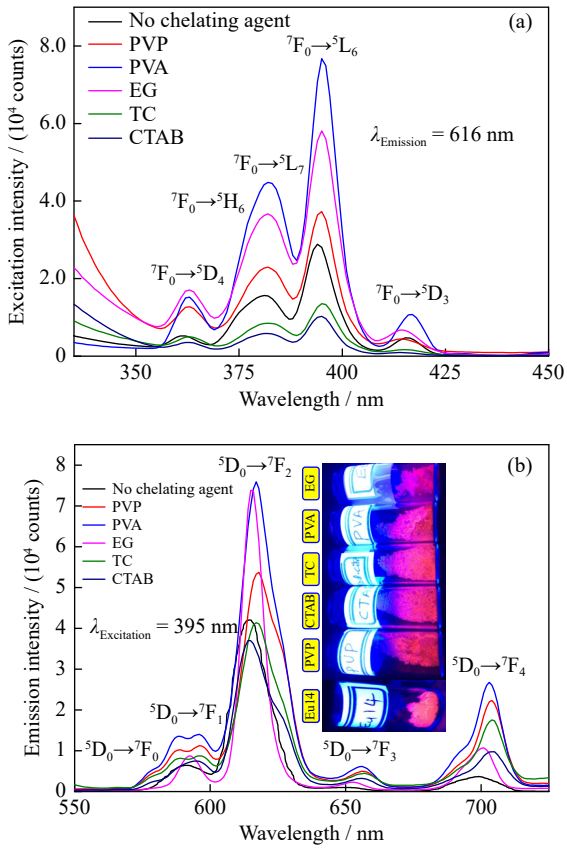

Fig. 6. (a) Excitation and (b) emission spectra of Eu^{3+} (14mol%)-doped LWO nanophosphors without and with PVP, PVA, EG, TC, and CTAB as chelating agents (Eu14 represents the sample without chelating agent).

Fig. 6(a). The photoluminescence emission spectra of Eu^{3+}-doped LWO nanophosphor samples synthesized without and with different chelating agents under identical conditions were acquired under excitation at 395 nm, as shown in Fig. 6(b). Characteristic emission peaks were observed at 578 nm ($^5D_0 \rightarrow {}^7F_0$), 587 nm ($^5D_0 \rightarrow {}^7F_1$), 616 nm ($^5D_0 \rightarrow {}^7F_2$), 655 nm ($^5D_0 \rightarrow {}^7F_3$), and 703 nm ($^5D_0 \rightarrow {}^7F_4$). The strongest emission band was at 616 nm ($^5D_0 \rightarrow {}^7F_2$) under 395 nm excitation [48]. Significantly, the Eu^{3+} (14mol%)-doped LWO nanophosphors synthesized using the PVA chelating agent demonstrated superior emission performance compared with those synthesized using the other chelating agents, as depicted in Fig. 6(b). This predominance is attributed to the combined effect of the optimal particle morphology, reduced surface defects, and effective incorporation of Eu^{3+} into the host lattice. The luminescence transitions are clearly demonstrated in the energy-level scheme diagram in Fig. 7.

Examination of the emission spectra of Eu^{3+} (14mol%) in the $La_{10}W_{22}O_{81}$ nanophosphors synthesized with different chelating agents (PVP, PVA, EG, TC, and CTAB) revealed slight shifts in the emission band positions that were attributed to local environmental changes [49–50], structural changes in the host lattice, chemical interactions [51], and solvent effects [52]. The high surface-to-volume ratio of the nanophosphors suggested that surface-state modifications significantly influenced their luminescence properties. Chelating agents can modify these surface states, which lead to

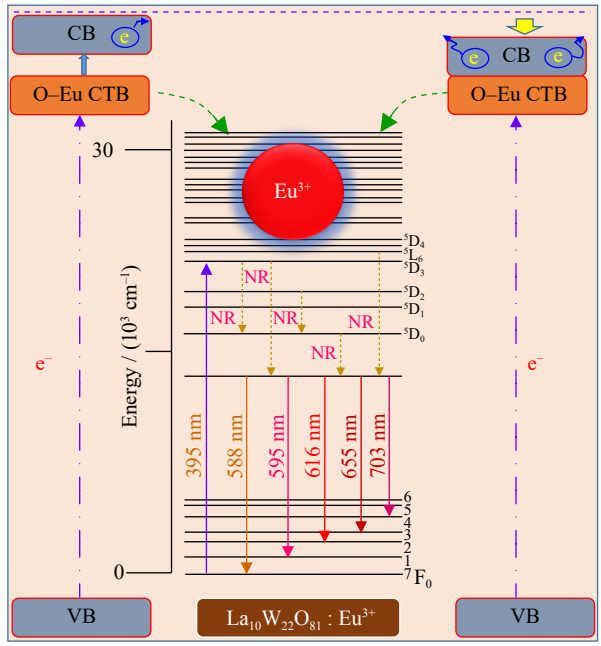

Fig. 7. Energy level scheme diagram for the photoluminescence of Eu^{3+} (14mol%)-doped LWO nanophosphor using PVA as chelating agent (CB is conduction band, VB is valancy band, and CTB is charge transfer band).

shifts in the emission bands by altering the ligand field around the Eu^{3+} ions, thereby affecting the splitting of the 4f electronic states and crystal field strength and symmetry [53–54]. However, the XRD analysis revealed no lattice distortions or secondary phases, indicating that structural effects did not contribute to the emission band shifts.

The hypersensitive transition of Eu^{3+} ions, specifically $^5D_0 \rightarrow {}^7F_2$, is significantly influenced by the local ligand field environment and thus serves as a valuable probe for determining the site symmetry. This electric dipole transition is generally more pronounced in lower symmetry sites, whereas the magnetic dipole transition, $^5D_0 \rightarrow {}^7F_1$, is characteristic of inversion symmetry sites [55]. The observed dominance of the electric dipole transition in the present study indicates that Eu^{3+} ions occupy sites that lack inversion symmetry within the host lattice. To further quantify the local symmetry, the asymmetry ratio (R_{21}) between the integrated intensities of the electric dipole ($^5D_0 \rightarrow {}^7F_2$) and magnetic dipole ($^5D_0 \rightarrow {}^7F_1$) transitions was calculated [56]. The R_{21} values for Eu^{3+} (14mol%)-doped $La_{10}W_{22}O_{81}$ nanophosphors with different chelating agents (PVP, PVA, EG, TC, and CTAB) were 4.77, 5.4, 8.45, 4.714, and 4.94, respectively, indicating the predominance of electric dipole transitions and accommodation of Eu^{3+} ions at non-centrosymmetric sites.

The luminescence decay behavior of Eu^{3+} (14mol%)-doped LWO samples, both pristine and surface-modified with various organic agents (PVP, PVA, EG, TC, and CTAB), was systematically studied, as shown in Fig. 8. The decay profiles were accurately fitted using a double-exponential function, suggesting the presence of multiple luminescence centers or energy transfer pathways within the host lattice. The pristine Eu^{3+}-doped LWO sample exhibited the longest maximum lifetime (τ_{max} = 0.62 ms), indicating effi-

cient suppression of non-radiative pathways [57]. Upon surface functionalization, a progressive reduction in the lifetime was observed, with τ_{max} values of 0.75 (PVA), 0.73 (EG), 0.65 (TC), and 0.64 ms (CTAB), respectively, as listed in Table 1. These variations clearly reflect the changes in the local crystal field environment and nonradiative deactivation probabilities introduced by the organic agents [58]. The longest τ_{max} for the PVA-modified sample indicates minimal disturbance to the host lattice and thus maximal preservation of the intrinsic Eu^{3+} luminescence properties. Conversely, the significant reduction in τ_{max} for the CTAB-functionalized sample points towards enhanced non-radiative relaxations, likely due to surface defects or increased phonon interactions arising from surfactant incorporation. The decay dynamics across all the samples were modeled using bi-exponential function [59]:

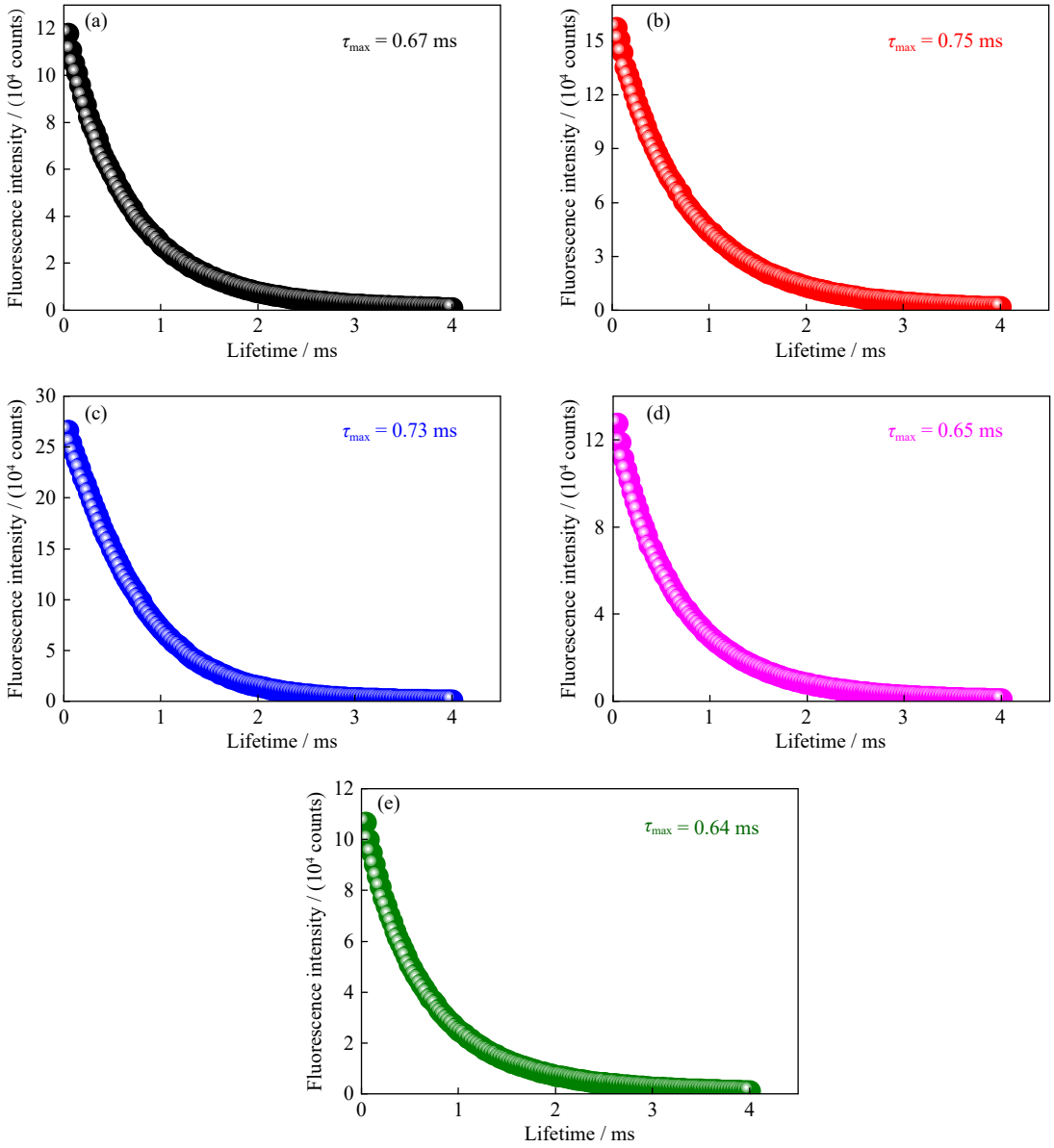

Fig. 8. Lifetime decay curves of Eu^{3+} (14mol%)-doped LWO nanophosphors with (a) PVP, (b) PVA, (c) EG, (d) TC, and (e) CTAB as chelating agent.

$$I(t) = A_1 \exp(-t/\tau_1) + A_2 \exp(-t/\tau_2) \quad (1)$$

where $I(t)$ denotes luminescence intensity at time t; τ_1 and τ_2 correspond to the values of the lifetime for the fast and slow exponential components, respectively; A_1 and A_2 are constants associated with the parameters for curve fitting. The average lifetime (τ_{avg}) was calculated using the following weighted relationship [60]:

$$\tau_{avg} = (A_1\tau_1^2 + A_2\tau_2^2)/(A_1\tau_1 + A_2\tau_2) \quad (2)$$

The observed decay trends suggest that Eu^{3+} ions are distributed in environments with varying symmetry and phonon coupling strengths, corroborating the hypothesis that heterogeneous emission sites exist. The systematic decline in τ_{max} further implies that the local structure and defect density critically influence the radiative decay processes, similar to the behavior reported for Eu^{3+}-doped $GdSr_2AlO_5$ nanophosphors [32].

Overall, these results highlight the sensitivity of the Eu^{3+}

Table 1. Lifetimes of the Eu^{3+} (14mol%)-doped LWO nanophosphors ([Eu:LWO]) synthesized using different chelating agents of PVP, PVA, EG, TC, and CTAB at excitation and emission wavelengths of 395 and 616 nm, respectively

Sample	ED/MD	Lifetime / ms	Adj. R^2
[Eu:LWO]	6.53	0.62	0.999
[Eu:LWO]/PVP	4.77	0.67	0.998
[Eu:LWO]/PVA	5.40	0.75	0.999
[Eu:LWO]/EG	8.45	0.73	0.997
[Eu:LWO]/TC	4.71	0.65	0.998
[Eu:LWO]/CTAB	4.94	0.64	0.999

Note: ED stands for electric dipole, MD stands for magnetic dipole transitions.

luminescence lifetime to surface modifications and provide insights into the tunability of emission properties for potential photonic and optoelectronic applications.

3.7. Colorimetry study

The international commission on illumination (CIE) chromaticity coordinates of the Eu^{3+} (14 mol%)-doped $La_{10}W_{22}O_{81}$ nanophosphors calculated from the emission spectra are critical parameters for luminescence applications. The obtained CIE coordinate results are listed in Table 2, along with the correlated color temperature (CCT) and color purity details. The CIE coordinates (0.6351, 0.3644) of the optimized PVA-assisted sample were in close agreement with those of the standard NTSC red phosphor [61] and the commercial Eu^{3+}-doped Y_2O_2S red phosphor (0.622, 0.351) [62]. The results in Fig. 9 suggest that the Eu^{3+}-doped $La_{10}W_{22}O_{81}$ nanophosphors prepared with PVA as chelating agent exhibit promising red emission characteristics under 395 nm excitation, making them suitable candidates for NUV white light-emitting diodes (WLED) and other photonic applications.

Table 2. CIE chromaticity coordinates, CCT, and color purity values of the Eu^{3+}-doped $La_{10}W_{22}O_{81}$ nanophosphors ([Eu:LWO]) synthesized using different chelating agents of PVP, PVA, EG, TC, and CTAB

Sample	CIE coordinates (x, y)	CCT / K	Color purity / %
[Eu:LWO]	(0.6277, 0.3269)	1018	86.4
[Eu:LWO]/PVP	(0.6551, 0.3446)	1000	99.2
[Eu:LWO]/PVA	(0.6351, 0.3644)	1147	99.6
[Eu:LWO]/EG	(0.6494, 0.3503)	1035	99.1
[Eu:LWO]/TC	(0.6472, 0.3525)	1052	99
[Eu:LWO]/CTAB	(0.6503, 0.3494)	1029	99.1

The color purity was evaluated using the following equation [63]:

$$\text{Color purity} = \frac{\sqrt{(x_s - x_i)^2 + (y_s - y_i)^2}}{\sqrt{(x_d - x_i)^2 + (y_d - y_i)^2}} \times 100\% \quad (3)$$

where (x_d, y_d), (x_s, y_s), and (x_i, y_i) are the chromaticity coordinates of the dominant wavelength, sample, and illuminant, respectively. In this study, (x_d, y_d) and (x_i, y_i) were determined to be (0.689, 0.329) and (0.33, 0.33), corresponding to the dominant wavelength of 616 nm.

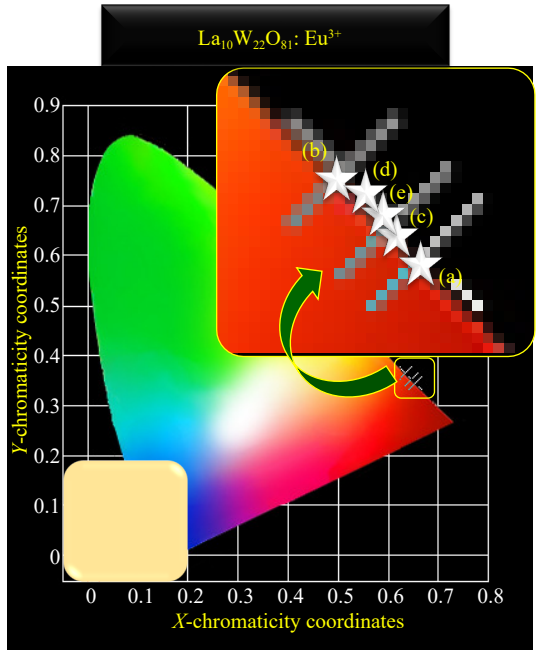

Fig. 9. CIE chromaticity diagram at an emission wavelength of 616 nm for the Eu^{3+} (14mol%)-doped LWO nanophosphors synthesized using various chelating agents.

As can be seen from Fig. 9 and Table 2, the PVA-assisted nanophosphors exhibited a high color purity of 99.6% with optimized CIE coordinates (0.6351, 0.3644), which is in good agreement with earlier reports [64–65]. These characteristics make the PVA-assisted nanophosphors highly suitable for warm WLED applications and photonic devices. The CCT, which describes the perceived color of light relative to a black-body radiator, was calculated using the McCamy empirical formula (Eq. (3)) [66]:

$$\text{CCT} = -499n^3 + 3525n^2 - 6823.3n + 5520.33 \quad (4)$$

where $n = (x - x_c)/(y - y_c)$ and (x_c, y_c) represents the chromaticity epicenter (0.3320, 0.1858). The calculated CCT values for the Eu^{3+}-doped LWO nanophosphors prepared with the different chelating agents indicate that these nanophosphors exhibit strong red emission characteristics, as shown in Fig. 9, making them suitable for warm white light applications.

3.8. Biocompatibility analysis

The long-term viability of nanomaterial-based products and technologies requires a thorough evaluation of their impact on human health and the environment. Essential to this assessment are cytotoxicity and biocompatibility studies, which should be conducted prior to application to ascertain any potential harmful effects. Therefore, we assessed the cytotoxicity of Eu^{3+} (14mol%)-doped $La_{10}W_{22}O_{81}$ nanophosphor with PVA as chelating agent. Using various doses, we examined their impact on C2C12 muscle myoblast cells over 48 h exposure period, following the detailed protocol described in the Supplementary Information. Fig. 10 presents the cytotoxicity trend of Eu^{3+} (14mol%)-doped $La_{10}W_{22}O_{81}$ nanophosphor with PVA as chelating agent via an in vitro CCK-8 assay. Fig. 10(a) and (b) shows the untreated and

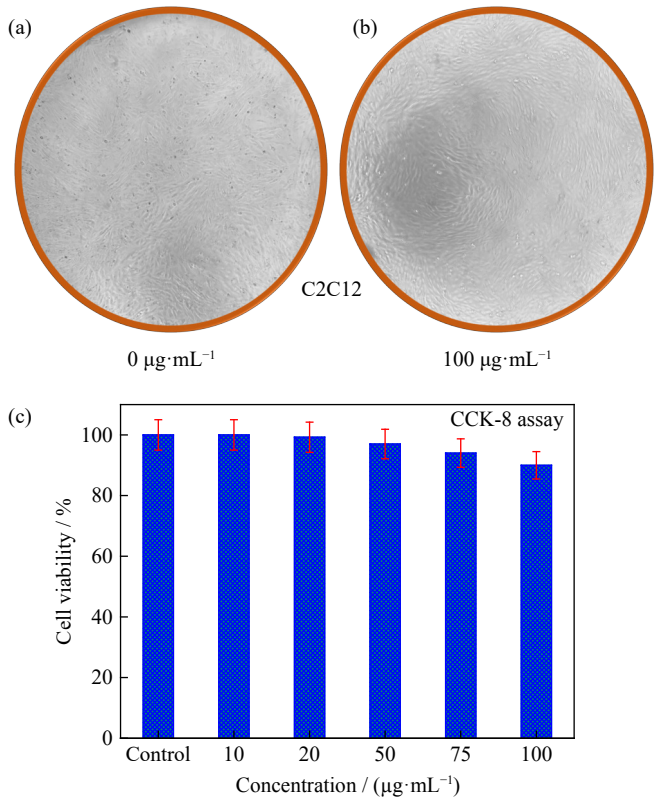

Fig. 10. (a, b) Untreated and treated cell viability assay micro-images of Eu^{3+} (14mol%)-doped $La_{10}W_{22}O_{81}$ nanophosphor with PVA as chelating agent in C2C12 mouse myoblast cells exposed for 48 h at different concentrations measured using the CCK assay and (c) cell viability trend by increasing the dosage concentration.

treated cell cultures, respectively, and reveals no significant morphological changes even at the highest dosage of 100 μg/mL.

The results indicated that the cell viability remained above 70% (approximately 91%) even at this high dosage, as depicted in Fig. 10(c). According to the ISO 10993-5:2009 standards [67], a material is considered cytotoxic if its cell viability falls below 70%. Therefore, the Eu^{3+} (14mol%)-doped $La_{10}W_{22}O_{81}$ nanophosphor with PVA as chelating agent promoted the proliferation of C2C12 cells, demonstrating its non-cytotoxic nature. The observed 10% cell death may be attributed to oxidative stress or other stimuli during exposure to the nanophosphors. Consequently, it shows promise as a biocompatible candidate for practical applications, even at high concentrations.

4. Conclusion

This study demonstrates that the red luminescence of Eu-doped lanthanum tungstate nanophosphors can be significantly enhanced by deliberate and systematic surface modification. XRD analysis confirmed an orthorhombic crystal structure, whereas SEM and TEM provided detailed insights into the particle size and morphology. The integration of characterization techniques such as FTIR and XPS enabled the identification of the surface functional groups and elucidated the ionic interactions in the samples. The use of surface modification agents (PVP, CTAB, TC, PVA, and EG) resulted in notable enhancements in the optical properties of the nanophosphors. Among these, the PVA-modified nanophosphors exhibited outstanding luminescence performance, achieving color purity of 99.6%, chromaticity coordinates of (0.6351, 0.3644), and CCT of 1147 K. These exceptional results were attributed to effective surface passivation and consequent suppression of nonradiative recombination, both of which are facilitated by the PVA modifier. Under UV excitation, the PVA-treated samples underwent pronounced red emission at 616 nm, corresponding to the $^5D_0 \rightarrow {}^7F_2$ transition of Eu^{3+} ions. Furthermore, the optimized sample exhibited an extended luminescence lifetime, highlighting its suitability for long-term performance in practical applications. Biocompatibility assessments revealed that the nanophosphors are environmentally benign and suitable for device fabrication without posing ecological risks. Overall, these findings confirm that PVA-modified Eu^{3+}-doped lanthanum tungstate nanophosphors are promising red-emitting candidates for next-generation photonic devices, including WLEDs and latent fingerprint detection systems. This study underscores the pivotal role of surface modification in tailoring the luminescent properties and provides valuable insights into nanophosphor interface interactions, laying a molecular-level foundation for the development of advanced materials with superior optical performances for diverse technological applications.

Acknowledgements

The authors gratefully acknowledge the financial support provided by the National Research Foundation of Korea

(NRF) through the Basic Science Research Program, funded by the Ministry of Education (Nos. 2021R1A6A1A03039493 and 2022R1A2C1009389) and the authors extend their appreciation to the Researchers Supporting Project (No. RSPD2025R956), King Saud University, Riyadh, Saudi Arabia. The authors would like to sincerely thank Dr. Poonam Rani, Department of Physics, Tokyo Metropolitan University, Hachioji 192-0397, Japan, for her valuable suggestions and insightful discussions that greatly contributed to the improvement of this work.

Conflict of Interest

The authors declare that they have no known competing financial interests or personal relationships that could have appeared to influence the work reported in this paper.

Supplementray Information

Data availability The online version contains supplementary material available at https://doi.org/10.1007/ s12613-025-3212-9.

References

[1] X.H. Zhu, J. Zhang, J.L. Liu, and Y. Zhang, Recent progress of rare-earth doped upconversion nanoparticles: Synthesis, optimization, and applications, *Adv. Sci.*, 6(2019), No. 22, art. No. 1901358.

[2] M.J. Song, W. Zhao, W.G. Ran, J.P. Xue, D. Kim, and J.H. Jeong, Synthesis, photoluminescence properties and potential applications of Eu^{3+} and Mn^{4+} activated $SrLaMgNbO_6$ phosphors, *Mater. Res. Bull.*, 122(2020), art. No. 110677.

[3] X.Y. Chen and X.Y. Huang, Efficient broadband yellow-emitting $Mg_{2.5}Lu_{1.5}Al_{1.5}Si_{2.5}O_{12}:Ce^{3+}$ garnet phosphors for blue-light-pumped white light-emitting diodes, *Ceram. Int.*, 50(2024), No. 1, p. 1022.

[4] L. Wang and R.J. Xie, Nitride and oxynitride phosphors for light emitting diodes, [in]: A. Kitai, ed., *Materials Solid State Lighting and Displays*iley, Hoboken, 2017, p. 135.

[5] R.J. Xie and N. Hirosaki, Silicon-based oxynitride and nitride phosphors for white LEDs—A review, *Sci. Technol. Adv. Mater.*, 8(2007), No. 7-8, p. 588.

[6] J. Grigorjevaite and A. Katelnikovas, Up-converting $K_2Gd(PO_4)(WO_4)$:20%Yb^{3+}, Ho^{3+} phosphors for temperature sensing, *Materials*, 16(2023), No. 3, art. No. 917.

[7] T. Pier and T. Jüstel, Application of Eu(III) activated tungstates in solid state lighting, *Opt. Mater. X*, 22(2024), art. No. 100299.

[8] F. Ayachi, K. Saidi, M. Dammak, J.J. Carvajal, and M.C. Pujol, Enhancing thermometric efficiency: A wavelength excitation analysis in $LiSrGdW_3O_{12}$: Tb^{3+} for superior single band ratiometric (SBR) thermometry, *RSC Adv.*, 14(2024), No. 19, p. 13494.

[9] S. Neeraj, N. Kijima, and A.K. Cheetham, Novel red phosphors for solid state lighting; the system $Bi_xLn_{1-x}VO_4$; Eu^{3+}/Sm^{3+} (Ln = Y, Gd), *Solid State Commun.*, 131(2004), No. 1, p. 65.

[10] C.F. Guo, L. Luan, C.H. Chen, D.X. Huang, and Q. Su, Preparation of $Y_2O_2S:Eu^{3+}$ phosphors by a novel decomposition method, *Mater. Lett.*, 62(2008), No. 4-5, p. 600.

[11] E. Sreeja, S. Gopi, V. Vidyadharan, *et al*., Luminescence properties and charge transfer mechanism of host sensitized $Ba_2CaWO_6:Eu^{3+}$ phosphor, *Powder Technol.*, 323(2018), p. 445.

[12] A. Heuer-Jungemann, N. Feliu, I. Bakaimi, *et al*., The role of ligands in the chemical synthesis and applications of inorganic nanoparticles, *Chem. Rev.*, 119(2019), No. 8, p. 4819.

[13] K.N. Kumar, L. Vijayalakshmi, J. Lim, and J. Choi, Dazzling green luminescent and biocompatible Tb^{3+}-activated lanthanum tungstate nanophosphors for group-III evaluation of latent fingerprints and anticancer applications, *J. Alloy. Compd.*, 959(2023), art. No. 170415.

[14] N.M. Zhang, C.F. Guo, J.M. Zheng, X.Y. Su, and J. Zhao, Synthesis, electronic structures and luminescent properties of Eu^{3+} doped $KGdTiO_4$, *J. Mater. Chem. C*, 2(2014), No. 20, p. 3988.

[15] S.K. Gupta, M. Abdou, P.S. Ghosh, *et al*., On comparison of luminescence properties of $La_2Zr_2O_7$ and $La_2Hf_2O_7$ nanoparticles, *J. Am. Ceram. Soc.*, 103(2020), No. 1, p. 235.

[16] X. Min, Y.K. Sun, L.T. Kong, *et al*., Novel pyrochlore-type $La_2Zr_2O_7:Eu^{3+}$ red phosphors: Synthesis, structural, luminescence properties and theoretical calculation, *Dyes Pigm.*, 157(2018), p. 47.

[17] H. Yi, J.W. Che, Z.H. Xu, G.Y. Liang, and X.Y. Liu, Sintering resistance of $La_2Ce_2O_7$, $La_2Zr_2O_7$, and yttria stabilized zirconia ceramics, *Ceram. Int.*, 47(2021), No. 3, p. 4197.

[18] J.M. Luo, Y. Wang, S.S. Chen, *et al*., Surface modification of Mg_2InSbO_6: Eu^{3+} phosphors and applications for white light-emitting diodes and visualization of latent fingerprint, *J. Alloy. Compd.*, 892(2022), art. No. 162049.

[19] C.H. Cheng, H.Y. Huang, M.J. Talite, W.C. Chou, J.M. Yeh, and C.T. Yuan, A facile method to prepare "green" nano-phosphors with a large Stokes-shift and solid-state enhanced photophysical properties based on surface-modified gold nanoclusters, *J. Colloid Interface Sci.*, 508(2017), p. 105.

[20] R. Sreedhara, B.R.R.rushna, B.D. Prasad, *et al*., A cost-effective intense blue colour cobalt doped gahnite pigment for latent finger print, cheiloscopy and anti-counterfeiting applications, *Colloids Surf., A*, 663(2023), art. No. 131038.

[21] B.N. Swathi, B.R.R. Krushna, S.A. Hariprasad, *et al*., Designing vivid green $Sr_9Al_6O_{18}:Er^{3+}$ phosphor for information encryption and nUV excitable cool-white LED applications, *J. Lumin.*, 257(2023), art. No. 119618.

[22] A.K. Pandey, K. Bankoti, T.K. Nath, and S. Dhara, Hydrothermal synthesis of PVP-passivated clove bud-derived carbon dots for antioxidant, catalysis, and cellular imaging applications, *Colloids Surf., B*, 220(2022), art. No. 112926.

[23] A.H. Monfared, A. Zamanian, M. Beygzadeh, I. Sharifi, and M. Mozafari, A rapid and efficient thermal decomposition approach for the synthesis of manganese–zinc/oleylamine core/shell ferrite nanoparticles, *J. Alloy. Compd.*, 693(2017), p. 1090.

[24] M. Khoeini, A. Najafi, H. Rastegar, and M. Amani, Improvement of hollow mesoporous silica nanoparticles synthesis by hard-templating method via CTAB surfactant, *Ceram. Int.*, 45(2019), No. 10, p. 12700.

[25] X.F. Wei, L.W. Li, H.G. Feng, J.B. Gong, K. Jiang, and S.L. Xue, Preparation and optical properties of In_2Se_3 nanospheres using CTAB as surface modifier, *Ceram. Int.*, 46(2020), No. 1, p. 1026.

[26] B.S. Li, H.H. Mao, X. Li, W. Ma, and Z.X. Liu, Synthesis of mesoporous silica-pillared clay by intragallery ammonia-catalyzed hydrolysis of tetraethoxysilane using quaternary ammonium surfactants as gallery templates, *J. Colloid Interface Sci.*, 336(2009), No. 1, p. 244.

[27] K.N. Kumar, L. Vijayalakshmi, P. Hwang, A.D. Wadhwani, and J. Choi, Bright red-luminescence of Eu^{3+} ion-activated $La_{10}W_{22}O_{81}$ microphosphors for noncytotoxic latent fingerprint imaging, *J. Alloy. Compd.*, 840(2020), art. No. 155589.

[28] K.N. Kumar, L. Vijayalakshmi, J. Lim, and J. Choi, Non-cytotoxic Dy^{3+} activated $La_{10}W_{22}O_{81}$ nanophosphors for UV based cool white LEDs and anticancer applications, *Spectrochim. Acta Part A*, 278(2022), art. No. 121309.

[29] M. Yoshimura and A. Rouanet, High temperature phase relation in the system La_2O_3–WO_3, *Mater. Res. Bull.*, 11(1976), No. 2, p. 151.

[30] J.P. Zuniga, S.K. Gupta, M. Abdou, and Y.B. Mao, Effect of

molten salt synthesis processing duration on the photo- and radioluminescence of UV-, visible-, and X-ray-excitable $La_2Hf_2O_7$:Eu^{3+} nanoparticles, *ACS Omega*, 3(2018), No. 7, p. 7757.
[31] C.F. Guo, F. Gao, Y. Xu, L.F. Liang, F.G. Shi, and B.H. Yan, Efficient red phosphors $Na_5Ln(MoO_4)_4$: Eu^{3+} (Ln = La, Gd and Y) for white LEDs, *J. Phys. D: Appl. Phys.*, 42(2009), No. 9, art. No. 095407.
[32] P. Kumar, D. Singh, and I. Gupta, UV excitable $GdSr_2AlO_5$:Eu^{3+} red emitting nanophosphors: Structure refinement, photoluminescence, Judd–Ofelt analysis and thermal stability for w-LEDs, *J. Alloy. Compd.*, 966(2023), art. No. 171410.
[33] M.T. Nguyen, P. Pattanasattayavong, and T. Yonezawa, Detailed discussion on the structure of alloy nanoparticles synthesized via magnetron sputter deposition onto liquid poly(ethylene glycol), *Nanoscale Adv.*, 6(2024), No. 7, p. 1822.
[34] A.K. Thottoli and A.K.A. Unni, Effect of trisodium citrate concentration on the particle growth of ZnS nanoparticles, *J. Nanostruct. Chem.*, 3(2013), No. 1, art. No. 56.
[35] R. Fenger, E. Fertitta, H. Kirmse, A.F. Thünemann, and K. Rademann, Size dependent catalysis with CTAB-stabilized gold nanoparticles, *Phys. Chem. Chem. Phys.*, 14(2012), No. 26, p. 9343.
[36] I.A. Safo, M. Werheid, C. Dosche, and M. Oezaslan, The role of polyvinylpyrrolidone (PVP) as a capping and structure-directing agent in the formation of Pt nanocubes, *Nanoscale Adv.*, 1(2019), No. 8, p. 3095.
[37] B.M. Song and C.W. Cho, Applying polyvinyl alcohol to the preparation of various nanoparticles, *J. Pharm. Invest.*, 54(2024), No. 3, p. 249.
[38] P. Narwal, M.S. Dahiya, A. Yadav, A. Hooda, A. Agarwal, and S. Khasa, Dy^{3+} doped LiCl–CaO–Bi_2O_3–B_2O_3 glasses for WLED applications, *Ceram. Int.*, 43(2017), No. 14, p. 11132.
[39] H. Najafi-Ashtiani, A. Bahari, S. Gholipour, and S. Hoseinzadeh, Structural, optical and electrical properties of WO_3–Ag nanocomposites for the electro-optical devices, *Appl. Phys. A*, 124(2018), No. 1, art. No. 24.
[40] Y. Yin, Y.N. Li, S.C. Liu, Y. Jiang, X.Y. Liu, and P. Zhang, Theoretical study of efficient photon–phonon resonance absorption in the tungsten-related vibrational mode of scheelite, *ACS Omega*, 9(2024), No. 9, p. 10517.
[41] R.T. Al-Mamari, H.M. Widatallah, M.E. Elzain, *et al.*, Core and surface structure and magnetic properties of mechano-synthesized $LaFeO_3$ nanoparticles and their Eu^{3+}-doped and Eu^{3+}/Cr^{3+}-co-doped variants, *Sci. Rep.*, 14(2024), No. 1, art. No. 14770.
[42] Y.R. Feng, K. Hu, M. Zhang, *et al.*, Engineering A-site cation deficiency into $LaCoO_3$ thin sheets for improved microwave absorption performance, *J. Mater. Sci.*, 57(2022), No. 1, p. 204.
[43] V. Guigoz, L. Balan, A. Aboulaich, R. Schneider, and T. Gries, Heterostructured thin $LaFeO_3$/g-C_3N_4 films for efficient photoelectrochemical hydrogen evolution, *Int. J. Hydrogen Energy*, 45(2020), No. 35, p. 17468.
[44] F.S. Manciu, J.L. Enriquez, W.G. Durrer, Y. Yun, C.V. Ramana, and S.K. Gullapalli, Spectroscopic analysis of tungsten oxide thin films, *J. Mater. Res.*, 25(2010), No. 12, p. 2401.
[45] D. Kim, S.C. Kim, J.S. Bae, S. Kim, S.J. Kim, and J.C. Park, Eu^{2+}-activated alkaline-earth halophosphates, $M_5(PO_4)_3X$:Eu^{2+} (M = Ca, Sr, Ba; X = F, Cl, Br) for NUV-LEDs: Site-selective crystal field effect, *Inorg. Chem.*, 55(2016), No. 17, p. 8359.
[46] D. Kim, Y.H. Jin, K.W. Jeon, *et al.*, Blue-silica by Eu^{2+}-activator occupied in interstitial sites, *RSC Adv.*, 5(2015), No. 91, p. 74790.
[47] P. Serna-Gallén, H. Beltrán-Mir, and E. Cordoncillo, Practical guidance for easily interpreting the emission and physicochemical parameters of Eu^{3+} in solid-state hosts, *Ceram. Int.*, 49(2023), No. 24, p. 41078.
[48] L. Liu, X.Y. Shao, Z.Y. Zhang, J.Y. Liu, Y.B. Hu, and C.F. Zhu, Spectral properties and self-reduction of Eu^{3+} to Eu^{2+} in aluminosilicate oxyfluoride glass, *RSC Adv.*, 13(2023), No. 34, p. 23708.
[49] Y.M. Hu, J.Y. Li, N.Y. Chen, C.Y. Chen, T.C. Han, and C.C. Yu, Correlation between defect-related photoluminescence emission and anomalous Raman peaks in N–Al co-doped ZnO thin films, *Appl. Phys. Lett.*, 110(2017), No. 14, art. No. 141903.
[50] A.U. Neelambra, C. Govind, T.T. Devassia, G.M. Somashekharappa, and V. Karunakaran, Direct evidence of solvent polarity governing the intramolecular charge and energy transfer: Ultrafast relaxation dynamics of push–pull fluorene derivatives, *Phys. Chem. Chem. Phys.*, 21(2019), No. 21, p. 11087.
[51] S.L. Zuo, P. Chen, and C.F. Pan, Mechanism of magnetic field-modulated luminescence from lanthanide ions in inorganic crystal: A review, *Rare Met.*, 39(2020), No. 10, p. 1113.
[52] J.R. Lakowicz, Solvent effects on emission spectra, [in] J.R. Lakowicz, ed., *Principles of Fluorescence Spectroscopy*, Springer, New York, 1999, p. 185.
[53] A.K. Singh, S.K. Singh, and S.B. Rai, Role of Li^+ ion in the luminescence enhancement of lanthanide ions: Favorable modifications in host matrices, *RSC Adv.*, 4(2014), No. 51, p. 27039.
[54] F. Travagin, M.L. Macchia, T. Grell, *et al.*, EHDTA: A green approach to efficient Ln^{3+}-chelators, *Dalton Trans.*, 53(2024), No. 4, p. 1779.
[55] Y. Kitagawa, J. Ueda, and S. Tanabe, A brief review of characteristic luminescence properties of Eu^{3+} in mixed-anion compounds, *Dalton Trans.*, 53(2024), No. 19, p. 8069.
[56] A.K. Parchur and R.S. Ningthoujam, Behaviour of electric and magnetic dipole transitions of Eu^{3+}, $^5D_0 \rightarrow {}^7F_0$ and Eu–O charge transfer band in Li^+ co-doped YPO_4:Eu^{3+}, *RSC Adv.*, 2(2012), No. 29, p. 10859.
[57] Y.M. Su, G.M. Wang, B.Y. Fu, X.X. Piao, and K.K. Zhang, A biomimetic phosphor that can build a rigid microenvironment for its long-lived afterglow in aqueous medium, *Commun. Chem.*, 7(2024), No. 1, art. No. 270.
[58] M.S.C. de Oliveira, A.J.S. Silva, W.S. Silveira, I. de F. Gimenez, and M.V. dos S. Rezende, Red emission enhancement in YVO_4: Eu^{3+} nanoparticle by changing the complexing agent in modified sol–gel route, *Opt. Mater.*, 138(2023), art. No. 113741.
[59] K.N. Kumar, L. Vijayalakshmi, J. Choi, and J.S. Kim, Efficient red-luminescence of $CaLa_2ZnO_5$ phosphors co-doped by Ce^{3+} and Eu^{3+} ions, *J. Alloy. Compd.*, 787(2019), p. 711.
[60] S. Slimi, P. Loiko, A. Volokitina, *et al.*, Structure, optical properties and preferential site substitution of Eu^{3+} activated $Ca_8NaBi(PO_4)_6F_2$ red emitting phosphors prepared by modified Pechini process, *J. Lumin.*, 241(2022), art. No. 118523.
[61] J. Liang, L.L. Sun, G. Annadurai, *et al.*, Synthesis and photoluminescence characteristics of high color purity $Ba_3Y_4O_9$:Eu^{3+} red-emitting phosphors with excellent thermal stability for warm W-LED application, *RSC Adv.*, 8(2018), No. 56, p. 32111.
[62] Y.L. Yao and Z.F. Zhou, Photoluminescence characteristics of a novel red phosphor $Ba_2Si_4O_{10}$:Eu^{3+}: Structural effect and concentration quenching mechanism, *J. Lumin.*, 179(2016), p. 408.
[63] H. Gao, J.F. Zhao, Y. Zhang, *et al.*, Synthesis and photoluminescence of high color purity red-emitting $BaLaLiTeO_6$:Eu^{3+} phosphors, *J. Appl. Phys.*, 129(2021), No. 14, art. No. 143102.
[64] P. Pradhan and S. Vaidyanathan, Highly efficient red/orange-red emitting Eu^{3+} and Sm^{3+}/Eu^{3+} co-doped phosphors with their versatile applications, *Dalton Trans.*, 54(2025), No. 15, p. 6060.
[65] N. Ma, W. Li, B. Devakumar, and X.Y. Huang, Dazzling red-emitting europium(III) ion-doped $Ca_2LaHf_2Al_3O_{12}$ garnet-type phosphor materials with potential application in solid-state white lighting, *Inorg. Chem.*, 61(2022), No. 18, p. 6898.
[66] A. Dwivedi, M. Srivastava, A. Srivastava, C. Upadhyay, and S.K. Srivastava, Tunable photoluminescence and energy transfer of Eu^{3+}, Ho^{3+}-doped $Ca_{0.05}Y_{1.93-x}O_2$ nanophosphors for warm white LEDs applications, *Sci. Rep.*, 12(2022), No. 1, art. No. 5824.
[67] L.M. Antonini, T.L. Menezes, A.G. Dos Santos Jr, *et al.*, Osteogenic differentiation of bone marrow-derived mesenchymal stem cells on anodized niobium surface, *J. Mater. Sci. Mater. Med.*, 30(2019), No. 9, art. No. 104.